LETTER

Observation of moiré excitons in WSe_2/WS_2 heterostructure superlattices

Chenhao Jin[1,9], Emma C. Regan[1,2,9], Aiming Yan[1,3], M. Iqbal Bakti Utama[1,4], Danqing Wang[1,2], Sihan Zhao[1], Ying Qin[5], Sijie Yang[5], Zhiren Zheng[1], Shenyang Shi[1,6], Kenji Watanabe[7], Takashi Taniguchi[7], Sefaattin Tongay[5], Alex Zettl[1,3,8] & Feng Wang[1,3,8]*

Moiré superlattices enable the generation of new quantum phenomena in two-dimensional heterostructures, in which the interactions between the atomically thin layers qualitatively change the electronic band structure of the superlattice. For example, mini-Dirac points, tunable Mott insulator states and the Hofstadter butterfly pattern can emerge in different types of graphene/boron nitride moiré superlattices, whereas correlated insulating states and superconductivity have been reported in twisted bilayer graphene moiré superlattices[1–12]. In addition to their pronounced effects on single-particle states, moiré superlattices have recently been predicted to host excited states such as moiré exciton bands[13–15]. Here we report the observation of moiré superlattice exciton states in tungsten diselenide/tungsten disulfide (WSe_2/WS_2) heterostructures in which the layers are closely aligned. These moiré exciton states manifest as multiple emergent peaks around the original WSe_2 A exciton resonance in the absorption spectra, and they exhibit gate dependences that are distinct from that of the A exciton in WSe_2 monolayers and in WSe_2/WS_2 heterostructures with large twist angles. These phenomena can be described by a theoretical model in which the periodic moiré potential is much stronger than the exciton kinetic energy and generates multiple flat exciton minibands. The moiré exciton bands provide an attractive platform from which to explore and control excited states of matter, such as topological excitons and a correlated exciton Hubbard model, in transition-metal dichalcogenides.

A moiré superlattice can form between two atomically thin materials with similar lattices, and its period varies continuously with the twist angle between the constituent layers. The periodic moiré pattern introduces a new length and energy scale, which provides a powerful means of controlling quantum phenomena in 2D heterostructures[1–12]. The most notable moiré superlattice phenomena emerge in the 'strong-coupling' regime, in which the periodic moiré potential dominates over the kinetic energy within the mini-Brillouin zone and qualitatively changes the electronic band structure and the electron wavefunction in the heterostructure. Recently, it was reported that strong-coupling moiré superlattices can generate flat electronic bands, which leads to exotic phases such as correlated insulating states and superconductivity in magic-twist-angle bilayer graphene and tunable Mott insulator states in trilayer graphene/boron nitride heterostructures[1–6].

Moiré superlattices also offer opportunities to engineer the band structure of collective excitations, such as excitons in 2D semiconducting heterostructures. Monolayer transition-metal dichalcogenides are direct bandgap semiconductors that feature strong light–exciton interactions and markedly enhanced electron–electron interactions in comparison to typical semiconductors such as silicon or gallium arsenide. Exciton-binding energies in monolayer transition-metal dichalcogenides can be hundreds of meV—orders of magnitude larger than those seen in typical semiconductors[16,17]—which leads to well-defined dispersive exciton bands in the Brillouin zone. It was recently predicted that moiré superlattices in heterostructures of transition-metal dichalcogenides in the strong-coupling regime could enable the formation of moiré exciton minibands[13–15], which are distinct from the separate electron and hole minibands owing to the strong electron–hole correlation.

Here we report the first experimental observation, to our knowledge, of moiré excitons in closely aligned WSe_2/WS_2 heterostructures. The moiré superlattice splits the WSe_2 A exciton resonance into multiple peaks that all exhibit comparable oscillator strengths in the absorption spectrum. Furthermore, the emergent exciton peaks show a dependence on doping that is distinct from both that of the A exciton in WSe_2 monolayers and that of WSe_2/WS_2 heterostructures with a large twist angle. This unusual behaviour can be understood by using an empirical model for moiré excitons with a peak-to-peak exciton moiré potential of 250 meV. The periodic potential energy is much larger than the exciton kinetic energy of 8 meV within the first mini-Brillouin zone and it completely changes the exciton dispersion in the moiré superlattice, which leads to flat low-energy exciton bands with highly localized exciton density of states. The closely aligned WSe_2/WS_2 moiré superlattice can therefore potentially host various excitonic states, such as topological exciton bands and a strongly correlated exciton Hubbard model[13–15,18,19].

Figure 1a, b shows an optical microscopy image and a side-view schematic of a representative WSe_2/WS_2 heterostructure device (D1). The results measured from device D1 were reproducible in all closely aligned heterostructures that we fabricated (see Supplementary Information). The WSe_2/WS_2 heterostructure was encapsulated in thin hexagonal boron nitride layers. Few-layer graphite flakes were used for both the bottom gate and the electrical contacts to the heterostructure. The carrier concentration in the heterostructure can be tuned continuously with the back-gate voltage V_G. All of the 2D materials used were first mechanically exfoliated from bulk crystals, then stacked together using a polyethylene terephthalate stamp according to a dry-transfer method (see Methods). The whole stack was then transferred onto a 90-nm silicon dioxide/silicon (SiO_2/Si) substrate. The relative twist angle between the WSe_2 and WS_2 layers was determined optically using polarization-dependent second-harmonic-generation measurements. Characteristic six-fold second-harmonic-generation patterns were clearly observed for the WSe_2 and WS_2 layers (Fig. 1c), from which we determined the relative twist angle between the two layers to be $0.5 \pm 0.3°$ (see Supplementary Information).
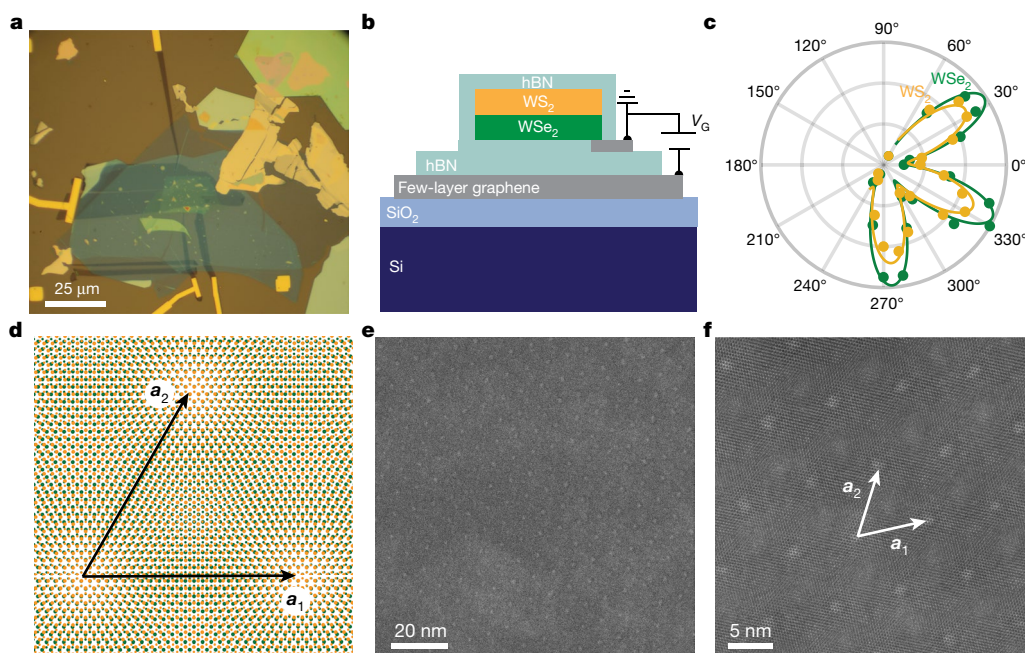
For a heterostructure with a near-zero twist angle, the lattice mismatch between the two layers is dominated by the intrinsic difference in lattice constant of about 4% (ref. [20]), which leads to a moiré periodicity L_M of approximately 8 nm (Fig. 1d, see also Supplementary Information). Similar moiré superlattices have been observed experimentally using scanning tunnelling microscopy in aligned WSe_2/MoS_2

[1]Department of Physics, University of California at Berkeley, Berkeley, CA, USA. [2]Graduate Group in Applied Science and Technology, University of California at Berkeley, Berkeley, CA, USA. [3]Material Science Division, Lawrence Berkeley National Laboratory, Berkeley, CA, USA. [4]Department of Materials Science and Engineering, University of California at Berkeley, Berkeley, CA, USA. [5]School for Engineering of Matter, Transport and Energy, Arizona State University, Tempe, AZ, USA. [6]Department of Physics, Fudan University, Shanghai, China. [7]National Institute for Materials Science, Tsukuba, Japan. [8]Kavli Energy NanoSciences Institute at University of California Berkeley and Lawrence Berkeley National Laboratory, Berkeley, CA, USA. [9]These authors contributed equally: Chenhao Jin, Emma C. Regan. *e-mail: fengwang76@berkeley.edu

Fig. 1 | Moiré superlattice in a WSe$_2$/WS$_2$ heterostructure with a twist angle close to zero. a, **b**, Optical microscopy image (**a**) and side-view illustration (**b**) of a representative heterostructure with a near-zero twist angle (device D1). **c**, The polarization-dependent second-harmonic-generation signal measured on the monolayer WSe$_2$ (green circles) and WS$_2$ (yellow circles) regions of device D1 and the corresponding fittings (green and yellow curves), which confirm the near-zero twist angle between WSe$_2$ and WS$_2$ layers. **d**, Illustration of the moiré superlattice in real space. The superlattice vectors, a_1 and a_2, have a length of

approximately 8 nm. **e**, **f**, Atomic-resolution scanning transmission electron microscopy high-angle annular dark-field image of another near-zero twist angle WSe$_2$/WS$_2$ heterostructure (device D2) (**e**) and a zoomed-in image (**f**). A well-defined triangular lattice pattern is observed over the whole measured region (**e**), with the two lattice vectors labelled (arrows in **f**). This corresponds to a periodic lattice distortion with a periodicity of around 8 nm, consistent with the formation of a moiré superlattice.

heterostructures[21,22], which have lattice constants that are almost identical to those of WSe$_2$/WS$_2$ heterostructures. To confirm the formation of the moiré superlattice in our WSe$_2$/WS$_2$ heterostructure, we prepared another device (D2) on a transmission electron microscopy grid and collected atomic-resolution scanning transmission electron microscopy images of the device (Methods), as shown in Fig. 1e, f. The images show a uniform triangular lattice pattern over the whole measured region (Fig. 1e) with a well-defined periodicity of about 8 nm (Fig. 1f). This indicates that a periodic lattice distortion with a periodicity of around

8 nm exists in the heterostructure in real space, which is consistent with the strong layer–layer interactions and substantial lattice reconstruction within the moiré superlattice that have been observed in previous scanning tunnelling microscopy studies[21,22].

We then studied the moiré excitons in WSe$_2$ with optical spectroscopy at a temperature of 10 K. Figure 2a shows the photoluminescence spectra of device D1 and a reference monolayer WSe$_2$ sample on both linear and logarithmic scales. The spectrum of the WSe$_2$/WS$_2$ heterostructure features a single peak at 1.409 eV, which corresponds to the
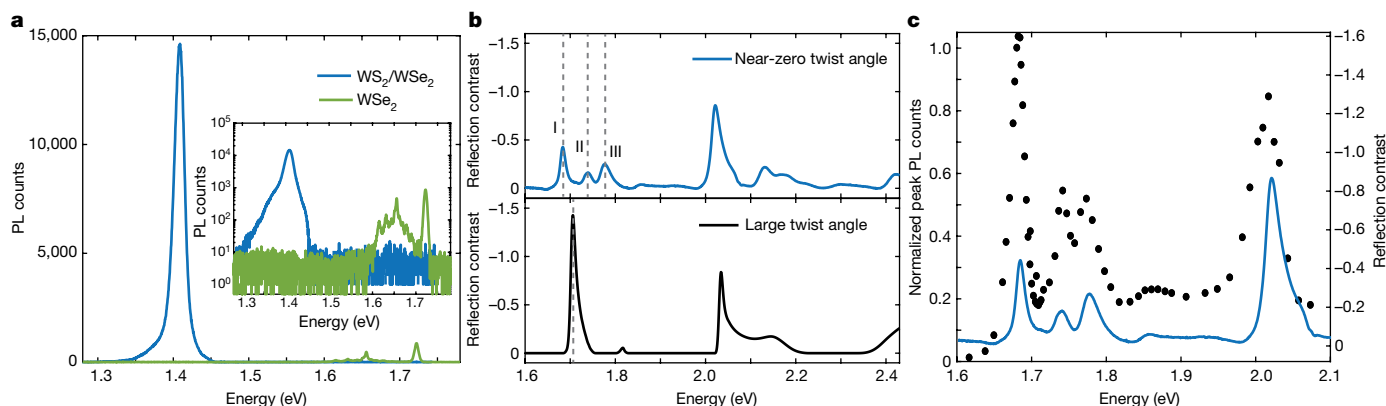
Fig. 2 | Moiré exciton states in a WSe$_2$/WS$_2$ moiré superlattice.
a, Photoluminescence (PL) spectrum of device D1 (blue) and a reference monolayer WSe$_2$ sample (green) on both linear (main image) and logarithmic (inset) scales. The complete disappearance of monolayer photoluminescence in the heterostructure indicates efficient interlayer coupling across the whole measured region. **b**, Reflection contrast spectrum of device D1 (light blue, top) compared to that of a WSe$_2$/WS$_2$ heterostructure with a large twist angle (black, bottom). The latter shows only a single resonance in the energy range 1.6–1.8 eV from the WSe$_2$ A

exciton state. By contrast, the moiré superlattice formed in device D1 gives rise to three prominent peaks with comparable oscillator strength in this range (labelled I to III), corresponding to distinct moiré exciton states. **c**, Comparison between the interlayer exciton photoluminescence excitation spectrum (black dots) and the reflection spectrum (blue curve). Strong enhancement of interlayer exciton photoluminescence is observed upon excitation at all moiré exciton states, indicating that all states are from the strongly coupled WSe$_2$/WS$_2$ heterostructure.
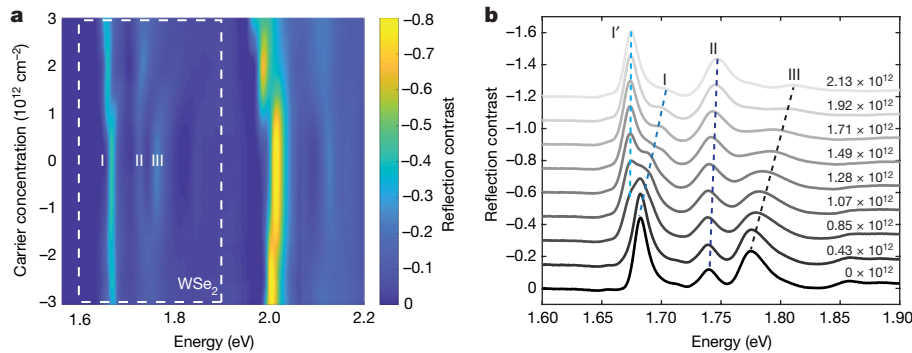
Fig. 3 | Doping dependence of the moiré exciton resonances. a, Gate-dependent reflection contrast spectrum of device D1 with both electron (positive carrier concentration) and hole (negative carrier concentration) doping. The white dashed box encloses the photon-energy range close to that of the WSe$_2$ A exciton, in which the three prominent moiré exciton states (labelled as I, II and III) appear. **b,** Detailed reflection contrast spectra in the range of the WSe$_2$ A exciton on the electron-doping side. The electron concentration, in units of cm^{-2}, is noted for each spectrum. Upon doping, peak I shows a strong blueshift and transfers its oscillator strength to another emerging peak at lower energy (I′), and peak III shows a strong blueshift with diminished oscillator strength. Peak II remains largely unchanged except for a small shift in energy.

emission from the interlayer exciton, and does not show any emission from the WSe$_2$ A exciton. This indicates an efficient interlayer charge transfer across the whole measured region that leads to strong quenching of the WSe$_2$ photoluminescence[23,24]. The exciton absorption in the same region of the heterostructure was directly measured using reflection contrast spectroscopy (Fig. 2b), in which a slowly varying background was subtracted to better resolve the resonances (see Supplementary Information). The absorption spectrum of device D1—a closely aligned heterostructure—is markedly different from that of a large-twist-angle WSe$_2$/WS$_2$ heterostructure measured under the same conditions (bottom panel in Fig. 2b). We focus on the WSe$_2$ resonances in the spectral range between 1.6 and 1.8 eV, because they are well separated from all WS$_2$ resonances. Whereas the large-twist-angle heterostructure shows only a WSe$_2$ A exciton peak at 1.715 eV, three prominent peaks emerge in the spectrum of device D1 at 1.683, 1.739 and 1.776 eV (labelled as resonances I, II and III, respectively). All three resonances show strong absorption, with the oscillator strengths of peaks II and III reaching 20% and 50%, respectively, of the value of peak I. We systematically investigated 18 different heterostructures that span a wide range of twist angles. The three emergent peaks are present in the spectra of all closely aligned devices for both AA stacking (0° twist angle) and AB stacking (60° twist angle). These peaks weaken with increasing twist angle between the WS$_2$ and WSe$_2$ layers, and disappear completely when the twist angle is larger than 3° (see Supplementary Information for twist-angle-dependent absorption spectra from 18 heterostructures).

To better understand these exciton peaks, we measured the photoluminescence excitation spectrum of the device D1 (Fig. 2c) by monitoring the intensity of the interlayer exciton emission as the excitation photon energy was swept from 1.6 to 2.1 eV. The excitation spectrum corresponds very well with the results from reflection spectroscopy (Fig. 2c). In particular, excitation at the energies of each of the three new exciton peaks between 1.6 and 1.8 eV led to strong enhancement of the interlayer exciton emission at 1.409 eV, which indicates that these peaks arise from the strongly coupled WSe$_2$/WS$_2$ heterostructure rather than from several separated domains.

To further investigate the nature of the emergent exciton resonances, we measured their dependence on doping of the heterostructure (Fig. 3a). The three main peaks in the range of the WSe$_2$ A exciton show pronounced changes upon both electron and hole doping. The strong gate-dependence upon electron doping is particularly notable: owing to the type-II band alignment in WSe$_2$/WS$_2$ heterostructures, doped electrons reside mostly in the WS$_2$ layers and tend to have relatively weak effects on the intralayer A exciton resonance in WSe$_2$ (refs. [25,26]; see also Supplementary Information). Previous studies of WSe$_2$/WS$_2$ heterostructures with large twist angles have shown that the WSe$_2$ A exciton resonance experiences only a slight redshift when

the heterostructure is doped with electrons[26]. By contrast, the exciton peaks in D1—a closely aligned heterostructure with a large moiré superlattice—show unusual dependencies on electron doping that vary for different peaks (Fig. 3b). Both peak I and peak III are substantially modified with increasing electron concentration: peak I shows a strong blueshift and transfers its oscillator strength to another emergent peak at lower energy (I′), and peak III shows a strong blueshift with diminished oscillator strength. Conversely, peak II remains largely unchanged except for a small shift in energy.

The strong effect of electrons in WS$_2$ on certain exciton transitions in WSe$_2$ indicates that interlayer electron–exciton interactions are markedly enhanced through the moiré superlattice. In addition, the substantially different gating behaviour of the exciton peaks cannot be explained by any established electron–exciton interactions in monolayers, such as dielectric screening effects or trion formation, because these affect all exciton peaks in a similar manner[27–29]. Instead, it indicates that exciton peaks I, II and III correspond to distinct exciton states within the moiré superlattice.

Both the emergence of multiple exciton peaks around the WSe$_2$ A exciton resonance and the nature of their electron-doping dependence can be understood in the context of an empirical theory that introduces a periodic moiré exciton potential in the strong-coupling regime. We follow the theoretical model in ref. [13] and describe the centre-of-mass motion of WSe$_2$ A excitons using the Hamiltonian

$$H = H_0 + \sum_{j=1}^{6} V_j \exp(i\boldsymbol{b}_j \cdot \boldsymbol{r}) \qquad (1)$$

in which H_0 is the low-energy effective Hamiltonian for the A exciton 1s state in monolayer WSe$_2$. V_j describes the effective potential on the exciton generated by the moiré pattern; its momentum is given by the reciprocal lattice vectors of the moiré superlattice, $\boldsymbol{b}_j$ (Supplementary Information). Owing to the three-fold rotational symmetry and Hermitian requirement, only one component in V_j is independent and can be defined as $V_1 = V\exp(i\psi)$, in which V and ψ are the amplitude and phase of the effective potential, respectively. We note that the peak-to-peak amplitude of the moiré potential V_{pp} can be much larger than V after summing the contribution from all six components.

The exciton dispersion in the mini-Brillouin zone can be directly calculated from this model (Fig. 4a–c). γ, m and κ are the high symmetry points of the mini-Brillouin zone, as illustrated in the inset of Fig. 4a. Without the moiré potential, the exciton shows two continuous bands at low energy (Fig. 4a). These two bands are degenerate at the point γ, and have parabolic and linear dispersion, respectively, as a consequence of the intervalley exchange interaction[13,30]. Because photons have negligible momentum, only the lowest-energy exciton can interact with light, giving a single strong peak at $E = E_0$ in the absorption spectrum
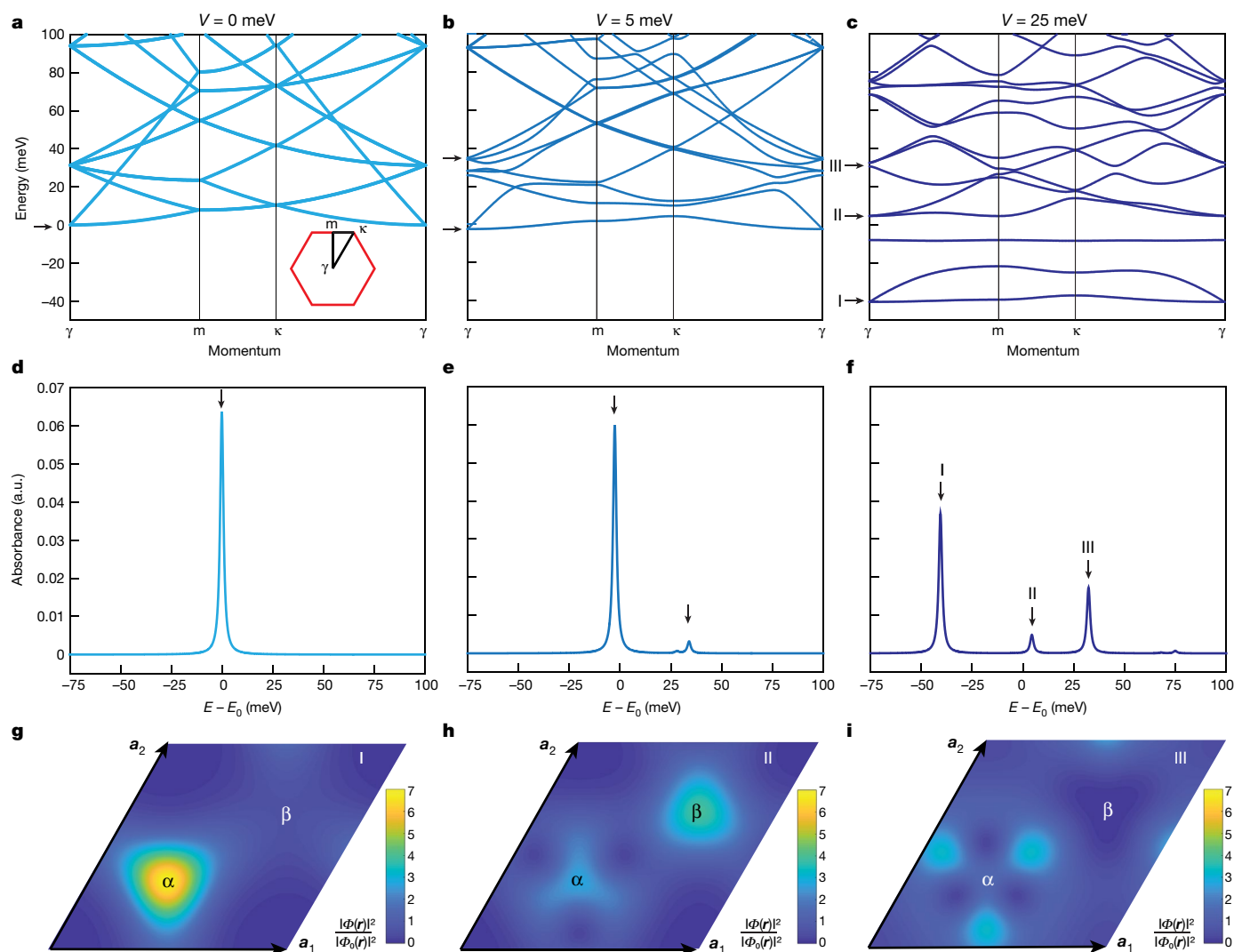
Fig. 4 | Moiré excitons in the strong-coupling regime. a–f, WSe$_2$ A exciton dispersion in the mini-Brillouin zone with a moiré potential parameter of $V = 0$ meV (zero coupling, **a**), 5 meV (weak coupling, **b**) and 25 meV (strong coupling, **c**), and the corresponding absorption spectra (**d–f**). A broadening of 2 meV was used in calculating the absorption spectrum. The inset in **a** illustrates the mini-Brillouin zone in momentum space and the high-symmetry points. Horizontal arrows in **a–c** label the optically active exciton states in each case that give rise to absorption peaks (vertical arrows in **d–f**). The absorption spectrum features a single resonance at energy E_0 at zero moiré potential (**d**), and shows a small side peak fixed at around 30 meV under a weak moiré potential (**e**). Conversely, the exciton dispersion is strongly modified in the strong-coupling regime owing to the strong mixing between different exciton states (**c**), which gives rise to multiple moiré exciton peaks with comparable oscillator strength in the absorption spectrum (peaks I–III in **f**) from different moiré minibands (states I–III in **c**). The experimentally observed reflection contrast can be reproduced by setting $V = 25$ meV and $\psi = 15°$. **g–i,** Real-space distribution of exciton centre-of-mass wavefunction in the strong-coupling regime. The strong moiré potential traps the lowest-energy exciton state I around its minimum point α (**g**). Notably, state III is also centred at point α, but state II is centred at a different point (**h, i**), which can account for the markedly different gate dependence observed for the different moiré exciton states.

(Fig. 4d). The moiré potential can mix exciton states with momenta that differ by b_j, which leads to additional absorption peaks from the γ-point states of higher-energy minibands.

When the moiré potential is weak ($V = 5$ meV, Fig. 4b), the exciton dispersion remains largely unchanged. Therefore, the emergent side peak in absorption always appears approximately 30 meV higher in energy than the main peak, regardless of the exact form of the moiré potential (Fig. 4e). Furthermore, the amplitude of the side peak is orders of magnitude smaller than that of the main peak, owing to the weak mixing between states. These features are in sharp contrast to the experimental absorption spectrum and cannot explain our observations. Conversely, a larger moiré potential that corresponds to the strong-coupling regime substantially modifies the exciton dispersion (Fig. 4c). As a result, the energy of the moiré exciton states in different minibands (labelled I to III in Fig. 4c), as well as the energy of

the corresponding absorption peaks (peak I to III in Fig. 4f), becomes highly dependent on the moiré potential. In addition, the strong mixing between different exciton states renders their oscillator strengths comparable with each other. If we set $V = 25$ meV and $\psi = 15°$, the simulated absorption spectrum can reproduce our experimental observation (Fig. 4f, see also Supplementary Information). This moiré potential has a peak-to-peak amplitude V_{pp} of around 250 meV, which is much larger than the exciton kinetic energy within the first mini-Brillouin zone (see Supplementary Information).

The substantial change in the exciton dispersion in momentum space suggests that the exciton centre-of-mass wavefunction is also strongly modified in real space. Figure 4g–i shows the distribution of the exciton probability density for states I to III in the moiré superlattice. The originally homogeneous wavefunction distribution is markedly changed by the moiré potential. For example, the lowest-energy state (state I) is

concentrated around the moiré potential minimum (labelled as point α) on a length scale that is much smaller than the moiré superlattice (Fig. 4g).

The unusual wavefunction distribution of moiré excitons in the strong-coupling regime introduces a new degree of freedom that is determined by the location of the exciton in the moiré superlattice. Notably, both peak I and peak III are centred around the same point, α, whereas peak II has its largest amplitude at a different point, β (Fig. 4h, i). The difference in real-space position between moiré exciton states can account for their differences in doping dependence: the doped electrons will also have localized density of states in real space[21,22]. If the gate-induced electrons in WS_2 are also localized at point α in the moiré superlattice, they will predominantly modify the exciton peaks I and III and peak II will remain largely unaffected, as observed experimentally.

We note that a complete description of the moiré exciton optical spectra will require a much more sophisticated model that fully accounts for the lattice relaxation and corrugation, as well as the hybridization of interlayer electronic states in the heterostructure moiré superlattice, which is beyond the scope of this study. The experimental investigation of interlayer moiré exciton states or obtaining spatially resolved optical measurements (such as by near-field nanoscopy) may provide further information for such models. Nevertheless, our simple moiré exciton model captures most of the salient features observed experimentally, and it shows that WS_2/WSe_2 heterostructures exhibit sufficiently strong interlayer interactions to enter the strong-coupling regime for excitons, in which the moiré excitons become spatially concentrated at well-separated points and form a quantum array in an extended moiré superlattice[13–15]. The substantially reduced exciton bandwidth also renders this artificial exciton lattice a promising platform for realizing exotic phases, such as a topological exciton insulator and a strongly correlated exciton Hubbard model.

Online content

Any methods, additional references, Nature Research reporting summaries, source data, statements of data availability and associated accession codes are available at https://doi.org/10.1038/s41586-019-0976-y.

1. Hunt, B. et al. Massive Dirac fermions and Hofstadter butterfly in a van der Waals heterostructure. *Science* **340**, 1427–1430 (2013).
2. Ponomarenko, L. A. et al. Cloning of Dirac fermions in graphene superlattices. *Nature* **497**, 594–597 (2013).
3. Dean, C. R. et al. Hofstadter's butterfly and the fractal quantum Hall effect in moiré superlattices. *Nature* **497**, 598–602 (2013).
4. Cao, Y. et al. Unconventional superconductivity in magic-angle graphene superlattices. *Nature* **556**, 43–50 (2018).
5. Cao, Y. et al. Correlated insulator behaviour at half-filling in magic-angle graphene superlattices. *Nature* **556**, 80–84 (2018).
6. Chen, G. et al. Gate-tunable mott insulator in trilayer graphene-boron nitride moiré superlattice. Preprint at https://arxiv.org/abs/1803.01985 (2018).
7. Shi, Z. W. et al. Gate-dependent pseudospin mixing in graphene/boron nitride moire superlattices. *Nat. Phys.* **10**, 743–747 (2014).
8. Spanton, E. M. et al. Observation of fractional Chern insulators in a van der Waals heterostructure. *Science* **360**, 62–66 (2018).
9. Wallbank, J. R., Patel, A. A., Mucha-Kruczynski, M., Geim, A. K. & Falko, V. I. Generic miniband structure of graphene on a hexagonal substrate. *Phys. Rev. B* **87**, 245408 (2013).
10. Song, J. C. W., Samutpraphoot, P. & Levitov, L. S. Topological Bloch bands in graphene superlattices. *Proc. Natl Acad. Sci. USA* **112**, 10879–10883 (2015).
11. Gorbachev, R. V. et al. Detecting topological currents in graphene superlattices. *Science* **346**, 448–451 (2014).
12. Lee, M. et al. Ballistic miniband conduction in a graphene superlattice. *Science* **353**, 1526–1529 (2016).
13. Wu, F., Lovorn, T. & MacDonald, A. H. Topological exciton bands in moiré heterojunctions. *Phys. Rev. Lett.* **118**, 147401 (2017).
14. Yu, H., Liu, G. B., Tang, J., Xu, X. & Yao, W. Moiré excitons: From programmable quantum emitter arrays to spin–orbit-coupled artificial lattices. *Sci. Adv.* **3**, e1701696 (2017).
15. Wu, F. C., Lovorn, T. & MacDonald, A. H. Theory of optical absorption by interlayer excitons in transition metal dichalcogenide heterobilayers. *Phys. Rev. B* **97**, 035306 (2018).
16. Chernikov, A. et al. Exciton binding energy and nonhydrogenic Rydberg series in monolayer WS_2. *Phys. Rev. Lett.* **113**, 076802 (2014).
17. Ye, Z. et al. Probing excitonic dark states in single-layer tungsten disulphide. *Nature* **513**, 214–218 (2014).
18. Greiner, M., Mandel, O., Esslinger, T., Hänsch, T. W. & Bloch, I. Quantum phase transition from a superfluid to a Mott insulator in a gas of ultracold atoms. *Nature* **415**, 39–44 (2002).
19. Fisher, M. P. A., Weichman, P. B., Grinstein, G. & Fisher, D. S. Boson localization and the superfluid-insulator transition. *Phys. Rev. B* **40**, 546–570 (1989).
20. Schutte, W. J., Deboer, J. L. & Jellinek, F. Crystal structures of tungsten disulfide and diselenide. *J. Solid State Chem.* **70**, 207–209 (1987).
21. Zhang, C. et al. Interlayer couplings, Moiré patterns, and 2D electronic superlattices in MoS_2/WSe_2 hetero-bilayers. *Sci. Adv.* **3**, e1601459 (2017).
22. Pan, Y. et al. Quantum-confined electronic states arising from the moiré pattern of MoS_2–WSe_2 heterobilayers. *Nano Lett.* **18**, 1849–1855 (2018).
23. Hong, X. et al. Ultrafast charge transfer in atomically thin MoS_2/WS_2 heterostructures. *Nat. Nanotechnol.* **9**, 682–686 (2014).
24. Wang, K. et al. Interlayer coupling in twisted WSe_2/WS_2 bilayer heterostructures revealed by optical spectroscopy. *ACS Nano* **10**, 6612–6622 (2016).
25. Kang, J., Tongay, S., Zhou, J., Li, J. B. & Wu, J. Q. Band offsets and heterostructures of two-dimensional semiconductors. *Appl. Phys. Lett.* **102**, 012111 (2013).
26. Jin, C. et al. Imaging of pure spin-valley diffusion current in WS_2-WSe_2 heterostructures. *Science* **360**, 893–896 (2018).
27. Wang, F. et al. Interactions between individual carbon nanotubes studied by Rayleigh scattering spectroscopy. *Phys. Rev. Lett.* **96**, 167401 (2006).
28. Raja, A. et al. Coulomb engineering of the bandgap and excitons in two-dimensional materials. *Nat. Commun.* **8**, 15251 (2017).
29. Mak, K. F. et al. Tightly bound trions in monolayer MoS_2. *Nat. Mater.* **12**, 207–211 (2013).
30. Yu, H., Liu, G. B., Gong, P., Xu, X. & Yao, W. Dirac cones and Dirac saddle points of bright excitons in monolayer transition metal dichalcogenides. *Nat. Commun.* **5**, 3876 (2014).

Author contributions F.W. and C.J. conceived the research. C.J., E.C.R. and D.W. carried out optical measurements. A.Y. and A.Z. performed electron microscopy measurements. C.J., F.W., E.C.R. and D.W. performed theoretical analysis. E.C.R., M.I.B.U., D.W., S.Z., Z.Z. and S.S fabricated van der Waals heterostructures. Y.Q., S.Y. and S.T. grew WSe_2 and WS_2 crystals. K.W. and T.T. grew hexagonal boron nitride crystals. All authors discussed the results and wrote the manuscript.

Competing interests The authors declare no competing interests.

METHODS

Preparation of the heterostructure for optical measurements. WSe_2/WS_2 heterostructures were fabricated using a dry-transfer method with a polyethylene terephthalate (PET) stamp[31]. Monolayer WSe_2, monolayer WS_2, few-layer graphene and thin hexagonal boron nitride (hBN) flakes were exfoliated onto silicon substrates with a 90-nm SiO_2 layer. Polarization-dependent second-harmonic generation was used to determine the relative angle between the WS_2 and WSe_2 flakes (see main text and Supplementary Information for details). A PET stamp was used to pick up the top hBN flake, the WS_2 monolayer, the WSe_2 monolayer, several few-layer graphene flakes for electrodes, the bottom hBN flake and the few-layer graphene back gate in sequence. The angle of the PET stamp was adjusted between picking up the WS_2 and the WSe_2 to assure a near-zero twist angle between the flakes. The PET stamp with the above heterostructure was then stamped onto a clean silicon substrate with 90 nm SiO_2, and the PET was dissolved in dichloromethane for 12 h at room temperature. The PET and samples were heated to 60 °C during the pick-up steps and to 130 °C for the final stamp process. Contacts (~75 nm gold with a chromium adhesion layer of ~5 nm) to the few-layer graphene flakes were made using electron-beam lithography and electron-beam evaporation.

Heterostructure preparation for electron microscopy. WS_2/WSe_2 heterostructures were prepared for (scanning) transmission electron microscopy ((S)TEM) characterization using a modified dry-transfer technique with a PET stamp. WS_2 monolayers, WSe_2 monolayers and thin hBN flakes were exfoliated and second-harmonic-generation measurements were used to determine flake orientation, as described above. A PET stamp was used to pick up the top hBN flake, the WS_2 monolayer and the WSe_2 monolayer in sequence. A Ted Pella Quantifoil TEM grid with 2-μm holes (657-200-AU) was placed on a silicon chip that was attached to the transfer stage. The PET stamp was lowered until it was in contact with the TEM grid, and then the temperature was raised to 80 °C until the stamp and the grid were well contacted, as seen through an optical microscope. The PET stamp and TEM grid were then placed in dichloromethane for 12 h at room temperature to dissolve the PET.

Atomic-resolution (S)TEM imaging. Atomic-resolution (S)TEM high-angle annular dark-field images of the h-BN/WS_2/WSe_2 heterostructure were taken under a double-aberration-corrected (S)TEM (TEAM 1 located at the National Center for Electron Microscopy, Lawrence Berkeley National Laboratory) operated at 80 keV. The semi-convergence angle was 30 mrad and the inner collection semi-angle was 70 mrad.

Data availability

The data that support the findings of this study are available from the corresponding author upon reasonable request.

31. Wang, L. et al. One-dimensional electrical contact to a two-dimensional material. *Science* **342**, 614–617 (2013).